

# Combining particle acceleration and coronal heating via data-constrained calculations of nanoflares in coronal loops

C. Gontikakis<sup>1</sup>, S. Patsourakos<sup>2</sup>, C. Efthymiopoulos<sup>1</sup>, A. Anastasiadis<sup>3</sup>, and M.K. Georgoulis<sup>1</sup>

<sup>1</sup>*Research Center for Astronomy and Applied Mathematics, Academy of Athens, Soranou Efessiou 4, 11528, Athens Greece*

[cgontik@academyofathens.gr](mailto:cgontik@academyofathens.gr)

<sup>2</sup>*Section of Astro-Geophysics, Department of Physics, University of Ioannina, 45110 Ioannina, Greece*

<sup>3</sup>*National Observatory of Athens, Institute for Astronomy, Astrophysics, Space Applications and Remote Sensing, GR-15236, Palaia Penteli, Greece*

## ABSTRACT

We model nanoflare heating of extrapolated active-region coronal loops via the acceleration of electrons and protons in Harris-type current sheets. The kinetic energy of the accelerated particles is estimated using semi-analytical and test-particle-tracing approaches. Vector magnetograms and photospheric Doppler velocity maps of NOAA active region 09114, recorded by the Imaging Vector Magnetograph (IVM), were used for this analysis. A current-free field extrapolation of the active-region corona was first constructed. The corresponding Poynting fluxes at the footpoints of 5000 extrapolated coronal loops were then calculated. Assuming that reconnecting current sheets develop along these loops, we utilized previous results to estimate the kinetic-energy gain of the accelerated particles and we related this energy to nanoflare heating and macroscopic loop characteristics. Kinetic energies of 0.1 to 8 keV (for electrons) and 0.3 to 470 keV (for protons) were found to cause heating rates ranging from  $10^{-6}$  to  $1 \text{ erg s}^{-1} \text{ cm}^{-3}$ . Hydrodynamic simulations show that such heating rates can sustain plasma in coronal conditions inside the loops and generate plasma thermal distributions which are consistent with active region observations. We concluded the analysis by computing the form of X-ray spectra generated by the accelerated electrons using the thick target approach that were found to be in agreement with observed X-ray spectra, thus supporting the plausibility of our nanoflare-heating scenario.

*Subject headings:* Sun: activity, Sun: corona, Sun: flares, Sun: magnetic topology

## 1. Introduction

A strong candidate mechanism to explain coronal heating is the formation of small-scale, still undetected, reconnection events, called nanoflares (Parker 1988). Reconnection events are sites where coronal magnetic energy is transformed into energy of accelerated particles eventually producing heating. Solar flares constitute a well documented case where accelerated particles, through reconnection, attain higher and higher kinetic energies, thus raising the plasma temperature while creating in the same time particle beams of supra-

thermal kinetic energies (Birn and Priest 2007).

Particle acceleration and the thermodynamic response of the plasma to heating are phenomena that were typically studied in isolation. In fact, a unifying study of particle acceleration, direct coronal heating and the thermodynamic response of the observed plasma structures such as coronal loops, seems hardly tractable, given the wide range of spatial and/or temporal scales involved. Indeed, these scales range from the dissipation scale (i.e. the scale of current sheet thickness), which is of the order of centimeters or meters, to

the scale of macroscopic phenomena taking place in the observed coronal structures which is of the order of several tens to  $\simeq 100$  Mm (Klimchuk 2006).

In the present work, we report on the results of an attempt to connect direct coronal heating, and its thermodynamic response, to particle acceleration. For this we use several simplifying assumptions in the theoretical and numerical treatment of each individual process considered. Furthermore, we empirically constrain our assumptions by exploiting available observational information, namely, measurements and estimates of the magnetic and the velocity field vectors in a particular active-region.

As a starting point we adopt Parker’s hypothesis (Parker 1972) that plasma motions at photospheric level stress, twist, and entangle the coronal magnetic field lines. This process converts the plasma kinetic-energy at the footpoints of coronal loops to non-potential (free) magnetic energy stored in the coronal magnetic fields. According to Parker (1988), when the magnetic field stress reaches a critical point, the stored free magnetic energy should be released to the plasma via reconnection events. For quantitative calculations, one equates the work rate done by the photospheric motions to the observed radiated energy in the corona, thus finding an estimate of the mean critical inclination of flux tubes, with respect to the direction normal to the solar surface, at which a reconnection event should take place. The resulting inclination angle, called the Parker angle, is derived through numerical simulations or analytical estimations. For active regions, it takes values in the range of  $5^\circ$  to  $20^\circ$  depending on the applied physical mechanism Galsgaard & Nordlund (1996); Klimchuk (2006); Rappazzo *et al.* (2007). The reason why the Parker angle appears preferentially in the above range (instead of taking values below  $1^\circ$  or around  $90^\circ$ ) has been interpreted in some numerical simulations as an effect of the temporal evolution of a reconnecting current sheet undergoing tearing instability (Dahlburg *et al.* 2005).

Numerical simulations can also help study how coronal magnetic fields are stretched and twisted due to photospheric plasma motions, thus developing complex, unstable current sheets (see,

for example, Galsgaard & Nordlund (1996)). In some cases it was found that there is a statistical equilibrium established between the energy supplied at the loop footpoints and the energy released throughout the whole structure of coronal loops via current sheets (Galsgaard & Nordlund 1996; Hendrix *et al.* 1996). The simulated current sheets are of various types, scales, and forms. In particular, they vary from large monolithic structures extending over the loop’s length (Galsgaard & Nordlund 1996) to cascades of smaller structures exhibiting a range of different sizes and spatial distributions (Galsgaard & Nordlund 1996; Hendrix *et al.* 1996; Rappazzo *et al.* 2007).

The above simulations show the dependence of the Parker angle on the loop parameters. However, they still present a high degree of idealization which may affect the computed Parker angle values. These include the simplified representation of the region between the photosphere and the corona (Klimchuk 2006), as well as the omission of the flux-tube divergence with height.

As our basic mechanism to explain the magnetic energy release during flares and nanoflares we adopt the acceleration of particles inside reconnecting current sheets. A crucial parameter toward achieving a viable simulation of this type is the ‘guide’ magnetic field, i.e. a magnetic field component parallel to the electric field that accelerates the particles. The main effect of the guide magnetic field is to change the *trajectories* of the charged particles, thus enhancing motion parallel to the electric field (Litvinenko & Somov 1993; Litvinenko 1996; Litvinenko 2000). In a previous work (Efthymiopoulos *et al.* 2005), these particles’ motions were studied for the case of a Harris-type reconnecting current sheet model by means of a Hamiltonian formalism. The result was a general formula predicting the maximum kinetic-energy gain of accelerated particles as a function of the initial energy of the particles and the parameters of the current sheet (thickness; field strengths). This formula is used in the present work to estimate the kinetic energy of the accelerated particles in the extrapolated coronal loops. We also note that, as found in Gontikakis *et al.* (2007) and Anastasiadis *et al.* (2008), the kinetic-energy distributions of accelerated particles through single or multiple current sheets (Harris type or X-point) are subject to upper limits due to the exis-

tence of a maximum possible kinetic energy gain of the particles.

Another input of our present analysis are estimates of the current sheet thicknesses encountered in these reconnection events. For this, we exploit results of recent particle-in-cell studies, in which the magnetic reconnection in solar flares takes place under the presence of a guide magnetic field (Hesse *et al.* 1999; Cassak *et al.* 2008). One then finds that the thickness of the diffusive current sheet is of the order of the electron gyro-radius.

Considering now the response of the coronal plasma to nanoflares, we rely on time-dependent hydrodynamic simulations (Patsourakos & Klimchuk 2005; Patsourakos *et al.* 2004). In these models, the cumulative effect of a large number of nanoflares, releasing energy in a coronal loop, is simulated in a way that allows direct comparison between simulations and observations from telescopes such as the *Transition Region and Coronal Explorer* (TRACE) (Handy *et al.* 1998) or, the *Atmospheric Imaging Assembly* (AIA, Lemen *et al.* (2012)) on board of the *Solar Dynamic Observatory* (SDO).

The structure of the paper is as follows: in Section 2 we discuss the observational data used to compute the structure of the magnetic field in the active-region corona. Section 3 presents our modeling of coronal loops, leading to a derivation of values for the field strengths and the footpoint velocities of the field lines forming the loops. Section 4 explains our main assumptions used to derive needed values of the current sheet parameters. Section 5 presents the particle acceleration results. These are used as an input to compute, in Section 6, the overall loop heating caused by particle acceleration. In Section 7 we present a simulation of how the X-Ray spectra of the accelerated electrons would look like under a thick-target model. Section 8 contains comprehensive results on loop heating via nanoflares, as well as on the thermodynamic response of the plasma in the modeled coronal loops. Section 9 offers a discussion of our results and of the limitations and validity of our modeling. Finally, Section 10 summarizes the basic conclusions of the present study.

## 2. Observations and data treatment

The Imaging Vector Magnetograph of the University of Hawaii’s Mees Solar Observatory recorded a timeseries of 12 vector magnetograms of the active region (AR) 09114 spanning over a  $\simeq 4.5$ -hour period on 8 August 2000 with a cadence of 20 minutes. These magnetograms have a field of view of  $280'' \times 280''$ , and a spatial resolution of  $0.55''$  (Mickey *et al.* 1996). The IVM recorded the Stokes vector of the Fe I 6302.5 Å photospheric spectral line.

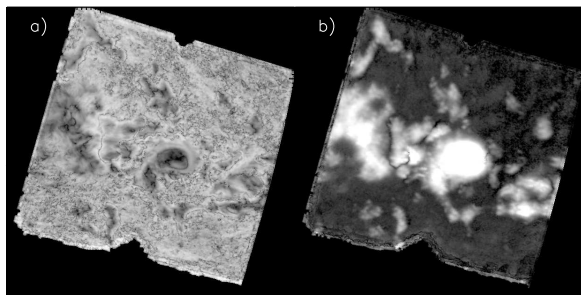


Fig. 1.— (a) The modulus of the velocity  $v = \sqrt{v_x^2 + v_y^2}$  computed with the MSR vector. The gray scale is set in the range from 0.3 to  $4.5 \text{ km s}^{-1}$ . (b) The modulus of the magnetic field from the vector magnetogram. The gray scale is set in the range from 10 to 500 Gauss.

Starting from the above data, we first resolve the azimuthal 180-degree ambiguity in each magnetogram using the Non-potential Magnetic Field Calculation (NPFC) method of Georgoulis (2005), as refined in Metcalf *et al.* (2006). Then, we compute a mean vector magnetogram as well as a map of the associated photospheric horizontal velocity, calculated by means of the Minimum Structure Reconstruction (MSR) technique (Georgoulis & Labonte 2006) (see Figure 1).

Expressing the photospheric magnetic field vector in the local heliographic reference system, we can now perform a current-free (potential) field extrapolation using the method proposed by Alissandrakis (1981). This computation was done in a cube up to an altitude of  $70''$ , or  $\simeq 50 \text{ Mm}$ , while the potential field extrapolation was performed on a  $2 \times 2$  binned magnetogram.

### 3. Coronal loop modeling

Using the extrapolated potential fields, we now define the coronal loops and several associated quantities. We proceed via the following steps:

i) *Coronal loop identification.* We selected about 5000 extrapolated magnetic field lines all closing within the photospheric field of view. These magnetic field lines are identified as closed coronal loops. The loops' lengths (denoted  $L$  hereafter) range from 8 to 180 Mm. Loops' maximum heights range from 2.5 Mm to 50 Mm.

ii) *Magnetic field strength.* We computed a mean value  $\bar{B}$  of the magnetic field along each coronal loop as in Mandrini *et al.* (2000); Gontikakis *et al.* (2008). The mean magnetic field is found to statistically decrease with increasing loop length, with short loops ( $L < 20$  Mm) yielding an average  $\bar{B} \simeq 180$  G, while long loops ( $L > 100$  Mm), yield an average  $\bar{B} \simeq 60$  G. Figure 2a shows the mean magnetic field strength for each loop as a function of the loop's length.

iii) *Electric field strength.* For each coronal loop we calculate the photospheric electric field values at both footpoints  $\vec{E}_{phot} = -\frac{1}{c}\vec{v}_{phot} \times \vec{B}$  or

$$\vec{E}_{phot} = \frac{1}{c}(v_y B_z \vec{x} - v_x B_z \vec{y}) \quad (1)$$

In Equation 1,  $v_x$  and  $v_y$  are the calculated horizontal components of the photospheric velocities,  $B_z$  is the perpendicular magnetic field component and  $\vec{x}$ ,  $\vec{y}$  are the corresponding unit vectors. Equation (1) does not include  $v_z$  because, in the MSR method, the vertical (cross-field) velocity component is assumed to be negligible.

iv) *Poynting flux through loops and supply of free magnetic energy.* As an immediate consequence of (iii), we can deduce values of the Poynting flux normal to the solar surface at the loops footpoints. This is expressed as

$$\vec{S}_{foot} = \frac{c}{4\pi}(E_x B_y - E_y B_x)\vec{z} \quad (2)$$

where  $E_x = \frac{1}{c}v_y B_z$  and  $E_y = -\frac{1}{c}v_x B_z$  are the photospheric electric field components. For each loop, two Poynting fluxes  $\vec{S}_{foot1}$  and  $\vec{S}_{foot2}$  are computed at the positions of the respective footpoints (1 or 2). We should emphasize that, while we have the information about the direction of the velocity vectors at the points of the observational

grid, the local direction of small scale motions at the footpoints of each coronal loop is inaccessible. For this reason, we ignore signs indicating an in or out Poynting flux through the loop and define, instead, the absolute sum  $S_{phot} = |S_{foot1} + S_{foot2}|$  as a rough measure of the Poynting flux supplied to the loop due to photospheric motions. For a single, isolated loop, the supply of free magnetic energy should be considered as the result of the relative plasma motions at both footpoints, since both distort the magnetic field. In fact, this distortion results in currents developed inside the loops, whose magnetic field now becomes non-potential. Furthermore, Equation (2) is not exact as it does not precisely resolve the relative motions at the footpoints. However, it arguably gives the correct order of magnitude for the Poynting flux. Finally, Equation (2) neglects the changes of the magnetic field due to the emergence or submergence of magnetic flux (Harra *et al.* 2011). This is justified in the case of the AR 09114, since this is a fully developed and non-decaying active region at the time of the observations.

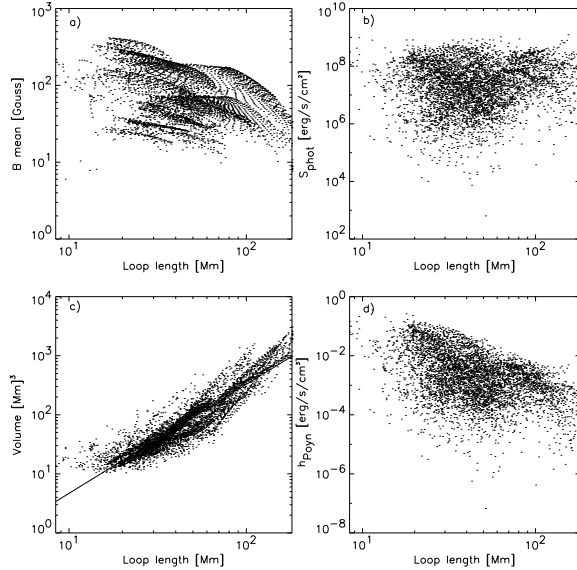


Fig. 2.— Scatter plots for several loop parameters as a function of the loop length. These are (a) the mean field strength, (b) the Poynting flux at both footpoints of each loop, (c) the loop volume, and (d) the volumetric heating rate due to Poynting flux. In panel (c) a fit is also shown.

The calculated  $S_{phot}$  (Figure 2b) has an average of  $7 \times 10^7 \text{ erg s}^{-1} \text{ cm}^{-2}$  and a standard deviation of  $\simeq 10^8 \text{ erg s}^{-1} \text{ cm}^{-2}$ . 95% of its calculated values are in the range  $5 \times 10^5$  to  $5 \times 10^8 \text{ erg s}^{-1} \text{ cm}^{-2}$ , regardless of the loop length. In Figure 2d we show the loop heating  $h_{Poynt}$  that would be produced if all the magnetic field energy input corresponding to the Poynting flux  $S_{phot}$  was converted to thermal energy. This quantity is computed for comparison with the heating terms derived using particle acceleration and presented in Section 6. As  $h_{Poynt}$  is an average value over time and space, it does not simulate the intermittent nature of nanoflares. It is given as

$$h_{Poynt} = \frac{A_{phot} (|S_{foot1}| + |S_{foot2}|)}{V_{loop}} \quad (3)$$

In Equation (3)  $A_{phot}$  is the cross-section at the footpoints of each loop, which is equal to the square of the magnetogram's binned pixel size, i.e.  $0.6 \text{ Mm}^2$ .  $V_{loop}$  is the loop volume (Figure 2c). Here,  $V_{loop}$  is calculated by integrating the volume of infinitesimal cylinders corresponding to the different cross-sections along the loop. We note that in subsequent calculations the cross-section is allowed to vary *along* each loop in order to conserve the magnetic flux passing through it. The constant magnetic flux of each loop equals the average magnetic flux calculated at its two footpoints. In Figure 2c, we performed a logarithmic fit which shows that the volume as a function of the loop length is described by  $V_{loop} = 0.07 L^{1.85}$ . This expression is used in Section 6 to describe a loop heating function.

In Figure 2d we see that  $h_{Poynt}$  is in the range of  $10^{-5}$  to  $0.4 \text{ erg s}^{-1} \text{ cm}^{-3}$ . Moreover,  $h_{Poynt}$  is decreasing as a function of loop length  $L$  due to the latter's inverse dependence on the loop volume  $V_{loop}$ . In the following,  $h_{Poynt}$  will be compared with the heating rates computed by the particles' acceleration.

We finally note that, instead of the sum  $|S_{foot1}| + |S_{foot2}|$ , we have also made calculations using  $|S_{foot1}| + |S_{foot2}|$  as an upper estimate of the total Poynting flux  $S_{phot}$  through a loop. Both expressions lead to quite similar results. Hereafter we will only refer to calculations performed by the choice  $|S_{foot1}| + |S_{foot2}|$ .

#### 4. Current sheet modeling

We now proceed to model current sheets formed along our extrapolated coronal loops. While a reasonable assumption is that each loop should include several current sheets at sub-resolution scales, it will be shown below that the resulting coronal heating by the cumulative result of multiple current sheets distributed inside the loop is equivalent to the heating from a single 'average' current sheet extending from footpoint to footpoint and consisting of a tangential discontinuity with a variable magnetic field vector across its surface. Figure 3 presents a schematic view of a stretched out cylindroidal coronal loop that contains one such current sheet. Since the magnetic flux is conserved along each loop, the loop's cross-section increases as we move from one of the footpoints towards the loop's apex. The current sheet is on the reconnection plane (dashed cut) which includes the cylindroid's axis. In Figure 3, the reconnection plane extends through the entire cylindroid. As shown in Section 5, this does not influence the resulting heating. The plane of the current sheet coincides with the plane of the discontinuity formed due to shearing motions at the photospheric level which presumably lead to the formation of two distinct magnetic-flux domains within the loop volume.

The magnetic field vectors in Figure 3 are depicted with different orientations above and below the reconnection plane. The angle  $\theta_D$  formed between two adjacent flux tubes at the discontinuity is assumed to be equal to twice the Parker angle.

These magnetic flux tubes, which form individual coronal loops, have a linear cross section smaller than 100 to 200 km (Cirtain *et al.* 2013; Chen *et al.* 2013). Our magnetogram data, binned to  $1.1''$ , cannot resolve these sub-resolution structures i.e. we cannot have any observational evidence on the value of the angle  $\theta_D$ . Given this limitation, in the present study we assigned a value of the angle  $\theta_D$  to each loop, picked from a uniform, distribution between  $8^\circ$  and  $50^\circ$ . The minimum value  $8^\circ$  corresponds to the upper limit of the mean inclination of magnetic fields in simulations of MHD-turbulence (Rappazzo *et al.* 2007) while the upper value includes (twice the) Parker angles of  $40^\circ$  and  $45^\circ$  derived from numerical simulations (Dahlburg *et al.* 2009; Galsgaard & Nordlund

1996). Moreover, it includes the typical value of  $40^\circ$  found from energy considerations (Klimchuk 2006). We also attempted to calculate  $\theta_D$  using the scaling law derived in Rappazzo *et al.* (2007). The results of the various calculations will be discussed in detail in section 6.

The shearing and twisting motions at the photospheric level are assumed such that the Poynting flux  $S_{phot}$  has a direction of injection inwards, i.e., into the sheet. For simplicity, we also assume that the current sheet is described by a Harris type geometry. In this geometry, two out of the three sheet's magnetic field components can be derived from the loop mean magnetic field  $\bar{B}$ , and  $\theta_D$ : i) the magnetic field component perpendicular to the loop axis and parallel to the current sheet plane is assumed to increase linearly with distance from the current sheet surface. Its maximum value  $B_{rec}$ , at the edges of the current sheet (see Figure 3), is given by  $B_{rec} = \bar{B} \sin(\theta_D/2)$ . ii) The magnetic field component parallel to the loop axis  $B_{\parallel}$  corresponds to the current sheet's guide field component. This component is assumed constant at each point inside the current sheet, and it is expressed as  $B_{\parallel} = \bar{B} \cos(\theta_D/2)$ . The dimensionless parameter  $\xi_{\parallel} = B_{\parallel}/B_{rec}$ , is important in current sheet literature (Efthymiopoulos *et al.* 2005; Litvinenko 2000). In the present modeling it is given by  $\xi_{\parallel} = \cot(\theta_D/2)$ . According to the above definitions, for  $\theta_D = 0$ , the tangential discontinuity vanishes as  $B_{rec} = 0$  and  $B_{\parallel} = \bar{B}$ . For  $\theta_D = \pi$ , we end up to an anti-parallel reconnection with  $B_{\parallel} = 0$  and  $B_{rec} = \bar{B}$ . For the adopted range of  $\theta_D$  between  $8^\circ$  and  $50^\circ$  we end-up with  $\xi_{\parallel}$  between 14.3 and 2.15 respectively. With the above settings, the injected Poynting flux  $S_{rec}$  is expressed by the energy conservation equation as

$$2 S_{rec} A_{rec} = A_{phot} (|S_{foot1}| + |S_{foot2}|) \quad (4)$$

In Equation (4),  $A_{rec}$  is the current sheet area and the factor 2 accounts for the fact that the Poynting flux is injected from both sides of the current sheet. Therefore, in Figure 3,  $A_{rec}$  corresponds to the area of the dashed current sheet.  $A_{rec}$  is calculated along each loop by integration, taking into account that the loop diameter normal to the loop's axis varies along the loop.  $A_{rec}$  takes values in the range from 10 to 760 Mm<sup>2</sup>, with longer loops exhibiting larger values of  $A_{rec}$ .

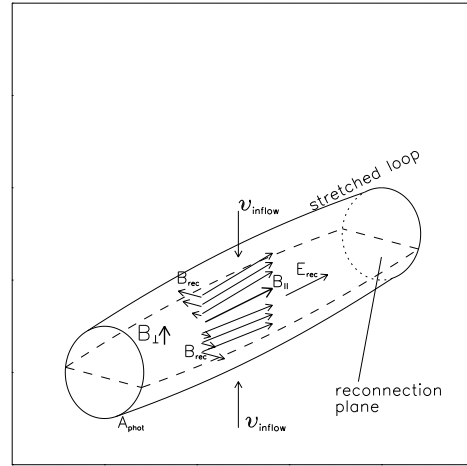


Fig. 3.— Stretched cylindroidal coronal loop. The lateral areas  $A_{phot}$  correspond to the loop foot-points. The current sheet is formed at a reconnection plane parallel to the cylindroid's main axis. The magnetic field changes orientation in the half-cylindroids defined by the reconnection plane. The magnetic field projection perpendicular to the cylinder's axis forms the reconnecting component  $B_{rec}$  while the projection parallel to the axis forms the parallel magnetic field component  $B_{\parallel}$ . The component  $B_{\perp}$  is perpendicular to the current sheet plane.

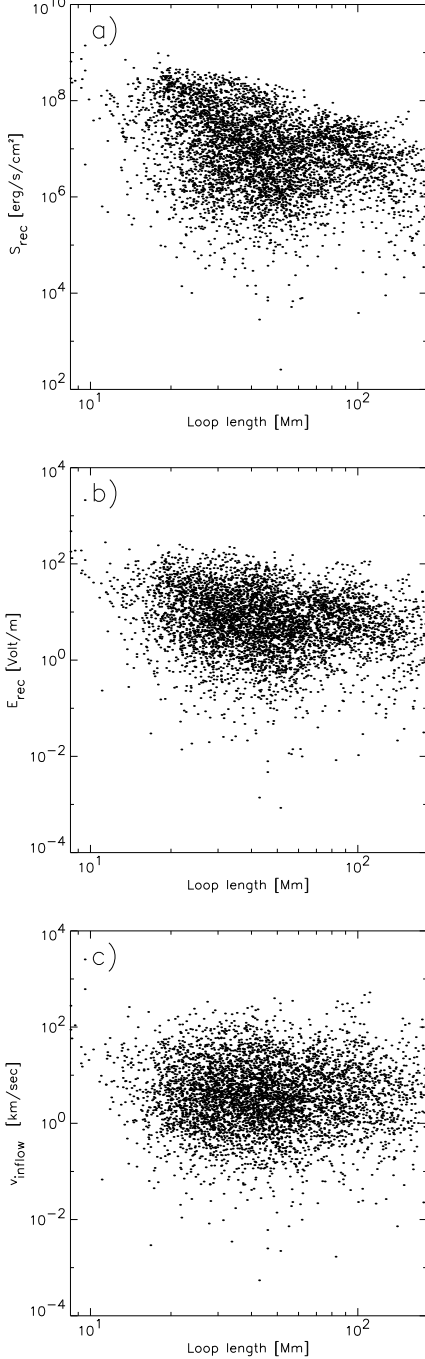


Fig. 4.— Scatter plots of (a) the Poynting flux injected (b) the reconnecting electric field, and (c) the plasma velocity inflow inside each of our considered current sheets.

The inflowing Poynting flux is directly related to the induced electric field  $\vec{E}_{rec}$  which accelerates particles inside the current sheet. The electric field is given by

$$\vec{E}_{rec} = -\frac{1}{c}(\vec{v}_{inflow} \times \vec{B}_{rec}) \quad (5)$$

where  $\vec{v}_{inflow}$  is the velocity of the plasma injected in the current sheet. The velocity  $\vec{v}_{inflow}$  can be derived from the expression of the injected Poynting flux  $S_{rec}$  via

$$\vec{S}_{rec} = \frac{c}{4\pi}(\vec{v}_{inflow} \times \vec{B}_{rec}) \times \vec{B}_{rec} \quad (6)$$

Figure 4 presents the results of the above calculations. Figure 4a shows that the injected  $S_{rec}$  values are in the range  $10^4$  to  $2 \times 10^9$  erg s<sup>-1</sup> cm<sup>-2</sup>. Furthermore,  $S_{rec}$  is decreasing with loop length because it is inversely proportional to  $A_{rec}$ . For short loops ( $L < 30$  Mm), the mean injected Poynting flux is  $S_{rec} \simeq 7.5 \times 10^7$  erg s<sup>-1</sup> cm<sup>-2</sup>, for intermediate size loops ( $30 \text{ Mm} < L < 100 \text{ Mm}$ ) we find  $S_{rec} \simeq 2.2 \times 10^7$  erg s<sup>-1</sup> cm<sup>-2</sup>, while for long loops ( $L > 100$  Mm)  $S_{rec} \simeq 7 \times 10^6$  erg s<sup>-1</sup> cm<sup>-2</sup>. Here we assume that, in an electron-proton plasma at thermal equilibrium, electrons will be accelerated practically without friction force (due to Coulomb interactions with the protons), because the electric field applied to the plasma is much larger than the Dreicer electric field computed for the standard coronal temperatures and plasma densities (Dreicer 1959; Benz 1993). In general, it is expected that electric fields appearing during solar-flare reconnection events are much larger than the Dreicer electric field (Martens & Young 1990). An explicit computation of the Dreicer field values of our model is given at the end of this section.

As seen in Figure 4b, 99% of the electric field values are between 0.01 and 100 V/m. The electric fields are also decreasing for increasing loop length. Moreover, 96% of the inflow velocity values (see Figure 4c) are in the range 0.1 to 100 km s<sup>-1</sup> but there appears to be no correlation between  $v_{inflow}$  and the loop length.

The next important parameter to compute is the magnetic field component  $B_{\perp}$  which is perpendicular to the plane of the current sheet (see Figure 3). Assuming consistency between the current derived from Ampère's law and the electric current

produced by the accelerated protons, considering that they carry most of the particle energy, one finds (Eastwood 1972; Martens & Young 1990; Litvinenko 1996) :

$$v_A B_\perp = \sqrt{2} v_{inflow} B_{rec} \quad (7)$$

where  $v_A$  is the Alfvén speed. The above equation is valid for  $\xi_\parallel = 0$ . In the absence of a guide component, the reconnecting component  $B_{rec}$  equals the average magnetic field  $\bar{B}$  so that, in Equation (7) the Alfvén speed can be expressed as  $v_A = B_{rec} / \sqrt{4\pi m_p n_e}$ . Equation (7) differs from the one found in Eastwood (1972), Martens & Young (1990), or Litvinenko (1996) by a factor  $\sqrt{2}$ . This numerical factor is introduced because we estimate the proton kinetic energy twice as much as in the above mentioned works, for reasons explained in Section 5. For  $\xi_\parallel \neq 0$ , on the other hand, the reconnecting field component is not equal to the mean magnetic field. Therefore,  $\bar{B}$  should replace  $B_{rec}$  in the Alfvén speed expression through the definition  $B_{rec} = \bar{B} \sin(\theta_D/2)$ . The term  $\sin(\theta_D/2)$  appears in Equation (7) which becomes:

$$v_A B_\perp = v_{inflow} B_{rec} \frac{\sqrt{2}}{\sin \frac{\theta_D}{2}} \quad (8)$$

Let us note that in the limit  $\theta_D = \pi$ , (anti-parallel reconnection), Equation (8) becomes identical to Equation (7).

In order to compute the Alfvén speed we use the Rosner *et al.* (1978) scaling-laws to determine the electron density for each loop assuming a maximum temperature of  $T_{max} = 10^6$  K. These scaling laws are valid in a strict sense for hydrostatic atmospheres. Their use in the present context will be commented in Sect. 9. Because of the relatively low value of  $T_{max}$  we have also low electron densities, i.e., in the range  $2 \times 10^8 \text{ cm}^{-3}$  up to  $6 \times 10^9 \text{ cm}^{-3}$ .

Figure 5a shows the Alfvén speed for all our current sheets. The values of  $v_A$  are in the range between  $10^3$  and  $1.6 \times 10^4 \text{ km s}^{-1}$  which are expected values for the coronal plasma. From Equation (8) we compute  $B_\perp$  for all the current sheets (Figure 5b), with 80% of the values in the range of 0.01 to 1 Gauss. The average  $B_\perp$  is 0.3 Gauss and its standard deviation 0.85 Gauss. Moreover, for the dimensionless quantity  $\xi_\perp = B_\perp / B_{rec}$ , 98% of the values are in the range of  $10^{-5}$  to 1.

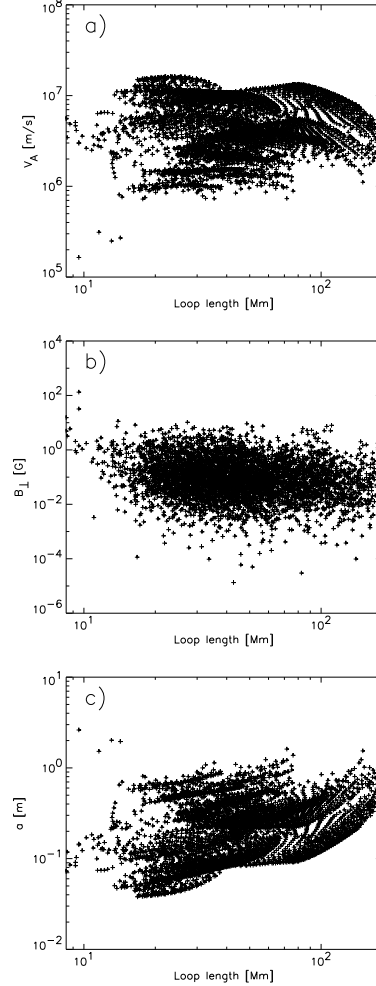


Fig. 5.— Scatter plots of (a) the Alfvén speed, (b) the perpendicular component  $B_\perp$ , and (c) the current sheet thickness, as a function of the loop length, for all current sheets considered.



Finally, we estimate the current sheet thickness as follows: according to Cassak *et al.* (2008), a current sheet becomes collisionless and susceptible to reconnection when its thickness  $a$  becomes of the order of the ion gyro-radius. However, when the guide magnetic field component is non-zero, the instability leading to reconnection occurs when the current sheet thickness becomes of the order of the Hall scale  $a = v_s(T)/\omega_{ci}$ , (Cassak *et al.* 2007), where  $v_s$  is the sound speed calculated for a plasma temperature  $T = 10^6$  K and  $\omega_{ci}$  is the ion-cyclotron frequency. The current sheet thickness can be also expressed as  $a = 5.69 \times 10^{-8} v_s \bar{B}^{-1} \frac{m_p}{m_e}$ . The resulting thickness turns to be of the order of the electron gyroradius. Figure 5c shows that the computed thicknesses in our current sheet sample range from 0.01 to 1 m, with the longer loops supporting thicker current sheets. Using the electron density  $n_e$  and temperature  $T = 10^6$  K we also calculated the Dreicer electric field, which is given by the expression  $E_D = 6.06 \times 10^{-6} n_e / T$  Volt/m (Benz 1993). Our computed electric fields  $E_{rec}$ , are larger than the Dreicer electric fields by factors ranging from 1 up to  $10^4$  for 97% of the cases. We conclude that the assumption of collisionless acceleration of the particles in our modeled current sheets is consistent with the adopted plasma parameters.

## 5. Particle acceleration

In this section we compute estimates of the kinetic energy gain of electrons and protons accelerated through the loop current sheets considered in the previous section. In our approach, charged particles enter the current sheet with a velocity  $v_{inflow}$  and are accelerated by the induced DC-electric field  $E_{rec}$ . Inside the current sheet, particles follow a trajectory which depends on the initial velocity and on the strength of the electric and magnetic fields. Particles are ejected before they can travel along the total length of the current sheet, which in our case is equal to the loop length, due to the Lorentz force raised by the  $B_\perp$  component (Speiser 1965). For current sheets with  $\xi_\parallel > 1$ , particles will follow adiabatic orbits with a very small amount of chaos (Efthymiopoulos *et al.* 2005). In the present study we did not examine the possibility that a particle interacts with more than one current sheet. Therefore, after the ejection from the

current sheet, particles move along the magnetic field lines without any further acceleration. The particles' kinetic energy gain is proportional to the electric field strength multiplied by the final acceleration length (along the electric field, see Fig. 3). As the electric fields  $E_{rec}$  are super-Dreicer, collisions are ignored. Therefore, to estimate the final kinetic energy one needs to compute the orbit as long as the particle is under the influence of the current sheet electric and magnetic fields. Efthymiopoulos *et al.* (2005) derived an analytical expression for the kinetic energy range  $E_k$  of accelerated particles inside a Harris type current sheet as a function of the initial particle energy  $E_{k0}$  and of the current sheet's parameters (field strengths and thickness). This expression reads

$$E_{kj} = E_{k0} + \frac{E_{rec}}{B_\perp^2} \left( e B_\parallel B_\perp a + m_j E_{rec} \pm \sqrt{2e m_j a B_\parallel B_\perp E_{rec} + m_j^2 E_{rec}^2 + 2 m_j B_\perp^2 E_{k0}} \right) \quad (9)$$

In Equation (9),  $j$  represents the particle species (electrons or protons). The two values for the  $\pm$  sign define the energy range around a mean kinetic energy. In the sequel we consider only the upper limit of the particles' kinetic energy range (plus sign in Equation 9). Furthermore we consider that the initial particle energies obey a Maxwellian distribution at a temperature of  $10^6$  K.

In Efthymiopoulos *et al.* (2005), the analytical expression is more cumbersome than in Eq. 9 as it includes explicitly  $I_2$ , an integral of the motion of particle orbits, resulting from the translational symmetry of the Harris type sheet geometry along  $\vec{E}_{rec}$  (see Figure 3 and Efthymiopoulos *et al.* (2005), Litvinenko & Somov (1993)). In Equation 9, we assume, for simplicity, that  $I_2 = 0$ . However, even with this restriction, Equation (9) gives a good estimate of the final kinetic energy of particles. The first two terms in Equation (9),

$$E_{ke} = E_{k0} + \frac{e E_{rec} B_\parallel a}{B_\perp} \quad (10)$$

are sufficient to describe the electrons average final kinetic energy (Litvinenko 2000) while for the protons, the kinetic energy is well described by the expression (Litvinenko 2000;

Efthymiopoulos *et al.* 2005)

$$E_{kp} = 2m_p c^2 \left( \frac{E_{rec}}{B_{\perp}} \right)^2 \quad (11)$$

where the factor 2 originates because in Equation (9) the  $m_p E_{rec}$  term is found twice and causes the  $\sqrt{2}$  factor in Equations 7,8. The initial particle kinetic energy, corresponding to a Maxwellian kinetic energy for the selected temperature of the order of 0.04 keV, is, on the average, 40 and 800 times smaller than the final kinetic energy of the electrons and protons respectively, after the acceleration process. The final electron kinetic energies are of the order 0.1 to 8 keV while final proton kinetic energies are in the range 0.3 keV to 470 keV (Figure 6).

Figure 6a, shows the kinetic energy distribution of electrons while Figure 6b shows the kinetic energy distribution of protons. The largest kinetic energies are found for loops with lengths ranging between 15 and 30 Mm. In Figures 6a,b the kinetic energy scatter plots for electrons and protons have a similar shape. This is because the kinetic energy of electrons depends on the Alfvén velocity while the kinetic energy of protons depends on the square of the Alfvén velocity. This dependence on the Alfvén velocity, which is implicit in Eqs 10,11 comes from the definition of  $B_{\perp}$  in Eq. 7. This dependence becomes explicit after the following calculation. Combining Equations (5),(6),(8),(10), (11) as well as the definitions of the thickness  $a$  and the  $B_{\parallel}$  component, we obtain the dependence of the sum of electron and proton kinetic energy gain on the initial parameters as :

$$\begin{aligned} E_k &= \frac{e E_{rec} B_{\parallel} a}{B_{\perp}} + 2 m_p c^2 \left( \frac{E_{rec}}{B_{\perp}} \right)^2 = \\ &= \frac{e}{c \sqrt{2}} \bar{B} \cos \frac{\theta_D}{2} a v_A \sin \frac{\theta_D}{2} + 2 m_p c^2 \left( \frac{v_A \sin \frac{\theta_D}{2}}{c \sqrt{2}} \right)^2 \\ \Rightarrow E_k &= \frac{e}{c 2 \sqrt{2}} c_1 v_s(T) v_A \sin \theta_D + m_p v_A^2 \sin^2 \frac{\theta_D}{2} \end{aligned} \quad (12)$$

Equation 12 holds for  $0 < \theta_D < \pi$  since for  $\theta_D = 0$  we have no current sheet while for  $\theta_D = \pi$  the reconnection is anti-parallel, ( $\xi_{\parallel} = 0$ ) and one should use Eq. 9. Moreover we omitted the initial kinetic energy  $E_{k0}$  from Eq. 12. In Equation 12, the constant  $c_1 = 5.8 \times 10^{-8} \frac{m_p}{m_e}$  originates from the

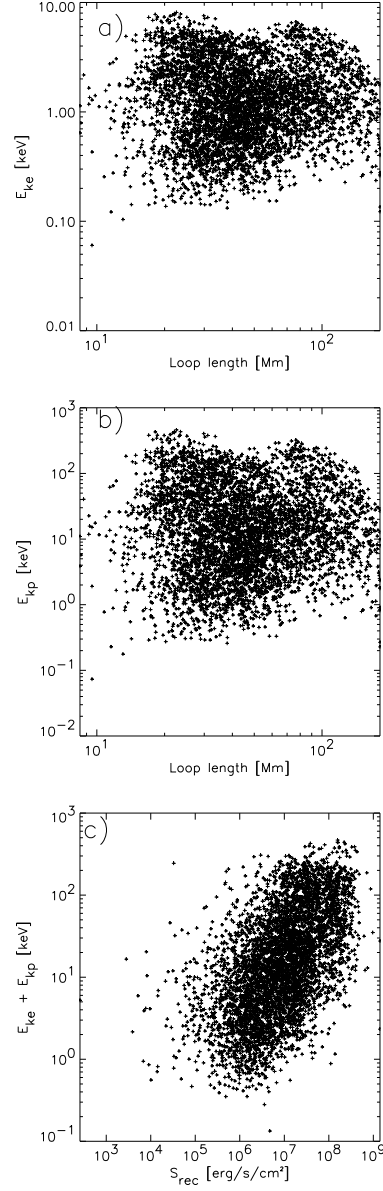


Fig. 6.— Scatter plots of the final kinetic energy for electrons (panel a), and protons (panel b). Panel c) shows the total kinetic energy of electrons and protons as a function of the Poynting flux entering the current sheet.

expression for the thickness  $a$  (Cassak et al 2007), introduced in Section 4. Equation (12) shows that the final kinetic energy  $E_k$  of the accelerated particles depends on the Alfvén velocity, the plasma density and the discontinuity angle  $\theta_D$ . The sound velocity  $v_s(T)$  is introduced through the thickness  $a$  of the current sheet. The kinetic energy  $E_k$  is implicitly related to  $S_{rec}$  as seen in Figure 6c, where we observe that  $S_{rec}$  and  $E_k$  are well correlated. Moreover, the electron kinetic energy as a function of the mean magnetic field at the loop footpoints is well fitted by power law  $E_{ke} \propto \bar{B}_{foot}^{0.65}$ . This means that for a different active region, with stronger photospheric magnetic fields, reaching, for example 5000 Gauss, we expect that electron kinetic energies can reach up to 10 keV. Another important aspect is that  $E_k$  is independent from the surface area  $A_{rec}$  of the current sheet. This means that the initial selection of the current sheet so as to cover the entire surface of the loop cross-section does not influence the resulting kinetic energies. This allowed us to choose, for each loop, a single current sheet with a simple geometry to describe particles' acceleration.

In addition, the acceleration length  $z_{max}$  of the particles is an important parameter in our model. The acceleration length is the distance along the electric field covered by the particles and it is defined via the expression  $E_k = e E_{rec} z_{max}$  for both particles species.  $z_{max}$  must obviously be smaller than the current sheet length or equivalently the coronal loop length. We found that for electrons, the ratio  $z_{max}/L$  is between  $10^{-7}$  and  $10^{-3}$  in 97% of the cases, while for protons it is between  $10^{-6}$  and 0.01 in 90% of the cases. For protons, the average value of  $z_{max}/L$  is  $10^{-3}$  with a standard deviation of 0.1. A short acceleration length relative to the loop length reduces the electric current intensity which, in turn, reduces the induced magnetic fields generated by the electric current of the accelerated particles (Martens & Young 1990; Litvinenko 1996).

We performed test particle simulations for the acceleration of electrons and protons similar to the ones presented in Gontikakis *et al.* (2007) and Anastasiadis *et al.* (2008). In these simulations, single particles, having initially a random  $10^6$  K thermal velocity, enter a Harris type current sheet with given initial parameters  $(a, B_{\parallel}, B_{\perp}, E_{rec}, B_{rec})$ . Solving the equations of

motion, a particle's orbit is traced until the particle leaves the current sheet, at half-width distance from the inversion surface. Running simulations for all 5000 current sheets used in this study is unrealistic, as they are time consuming. Therefore we selected 10 representative values of electric fields  $E_{rec}$ , reconnecting, parallel and perpendicular magnetic components  $(B_0, B_{\perp}, B_{\parallel})$  and current sheet thicknesses  $a$  from our calculated distributions. The resulting kinetic energies are in agreement with Equation (9). All 1000 electrons used in each simulation are accelerated to kinetic energies of the order inferred by Equation (10). However, most protons cross the current sheet with no energy gain and only roughly 10% of protons are accelerated. The accelerated protons are the ones having an initial velocity with a particular orientation relative to the current sheet. The fact that only a fraction of protons are accelerated was also found in Gontikakis *et al.* (2007).

To recapitulate, to estimate the particles' kinetic energies, we use observations of photospheric magnetic fields and inferences of the photospheric horizontal velocities. From them, we calculate the photospheric Poynting flux  $S_{phot}$  (Equation (2)). From a potential magnetic field extrapolation, we select 5000 closed loops, on each of which we calculate the mean magnetic field  $\bar{B}$ . From this, and by virtue of the assumptions described before, we calculate the parameters  $B_{rec}$ ,  $B_{\parallel}$ ,  $v_{inflow}$ ,  $E_{rec}$ ,  $a$  and  $B_{\perp}$  necessary and sufficient to calculate kinetic energies of accelerated particles.

## 6. Loop heating due to accelerated particles

We compute the heating of coronal loops assuming that it is produced solely by the ensuing thermalization of the accelerated particles. We assume that both electrons and protons participate in this process, since both particles' energy is released once they hit the dense chromospheric layer. Protons with energies ranging between 100 keV and 5 MeV can produce chromospheric evaporation thus participating in coronal heating (Emslie *et al.* 1996). In our simulation, only 10% of the protons' kinetic energies are above 100 keV. Nevertheless we assume that even protons with kinetic energy less than 100 keV participate in the loop heating.

The thermalization of the accelerated particles is a complex process which we do not model in detail. Instead, we use the following phenomenological expression for the heating rate :

$$Q = \frac{(E_{ke} + f E_{kp}) n_e}{t_{rec}} \frac{V_{rec}}{V_{loop}} \quad (13)$$

In Equation (13), the heating rate  $Q$  of a loop with a pre-nanoflare electron density  $n_e$ , corresponds to the thermalization of current-sheet accelerated electrons and protons to kinetic energies  $E_{ke}$  and  $E_{kp}$  respectively. A neutral, fully ionized plasma ( $n_e = n_p$ ) is assumed. Here  $V_{rec} = 2 v_{inflow} t_{rec} A_{rec}$  is the plasma volume injected inside the current sheets of total surface  $A_{rec}$  during the reconnection time  $t_{rec}$ . As reconnection time we define the duration of the reconnection event. The fraction  $V_{rec}/V_{loop}$  indicates that the heating produced inside the current sheets is redistributed to the loop volume  $V_{loop}$ . The efficiency factor  $f = 0.1$  means that only 10% of protons are accelerated, as found by the test particle simulations presented in the end of section 5.

In subsequent calculations we use Equations 4, 5, 12 and assume that the loop volume is  $V_{loop} = C_4 L^{-p}$ , where  $C_4 = 50.1$ ,  $L$  the loop length, and  $p = 1.85$  as found by the fit to the calculated loop volumes in Figure 2c. The heating  $Q$  is expressed (in  $\text{erg s}^{-1} \text{cm}^{-3}$ ) as :

$$Q = \frac{4\pi}{c} \left( \frac{e}{c 2\sqrt{2}} c_1 \sin \theta_D v_s(T) v_A + f m_p v_A^2 \sin^2 \frac{\theta_D}{2} \right) \frac{n_e \bar{S}_{foot} A_{phot}}{B_{rec}^2 C_4 L^p} \quad (14)$$

Here  $\bar{S}_{foot} A_{phot}$  is the average photospheric Poynting flux times the footpoint cross-section. In Equation (14) we can see that the heating rate  $Q$  does not depend on  $t_{rec}$  and that the electron and proton terms have a different form of dependence on  $v_A$ . We can also express  $Q$  as a function of  $L$  if we replace the electron density  $n_e$  by the expression given in Rosner *et al.* (1978). The individual heating rates due to electrons and protons have a power law dependence on  $L$  but with a slightly different exponent

$$Q_e \propto \bar{S}_{foot} \frac{\cot \frac{\theta_D}{2} T v_s(T)}{B L^{\frac{1+2p}{2}}} \quad (15)$$

$$Q_p \propto \bar{S}_{foot} \frac{1}{L^p} \quad (16)$$

Figure 7 shows the heating rates due to electrons

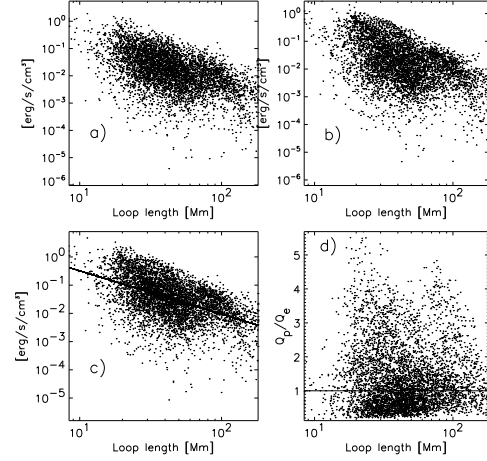


Fig. 7.— Heating rates produced by electrons (panel a), protons (panel b), and by both particle types (panel c) as a function of loop length. Panel d shows the ratio of proton heating over electron heating as a function of loop length. Panel c) also shows a linear fit to the log of the heating rate distribution.

(Figure 7a), protons (Figure 7b) and both types of particles (Figure 7c) as a function of loop length. Despite the larger scatter, the similar power law dependence of the heating produced by each type of particles, shown in Equation (15), is also visible in the scatter plots of Figure 7a-c. The heating-flux ratio  $Q_p/Q_e$  seen in Figure 7d takes values in the range 0.1 to 5 with 50% of the values larger than 1. The heating rate function from the two particle species (Figure 7c) is in the range of  $10^{-4}$  to  $1 \text{ erg s}^{-1} \text{cm}^{-3}$ . We also show a linear fit to the logarithm of the values in the scatter plot. The calculated power law index is of  $c_2 = -1.5$ . This index differs from  $p = 1.85$ , the exponent of  $L$  in Equation (15). The reason is that  $\bar{S}_{foot}$ , which appears in Equation (15) has also a weak dependence on  $L$ , with a positive power law index  $a = 0.35$ , which influences the resulting fit. In Mandrini *et al.* (2000), the heating rate deduced from loops observed in X-rays with the SXT telescope on Yohkoh has a power law relation with the loop length, with exponents in the interval  $[-4.5, -1]$  and most probable value  $\simeq -2$ . Therefore, the exponent value of  $-1.5$  presently derived is fairly consistent with observations. In Figure 8, we plot

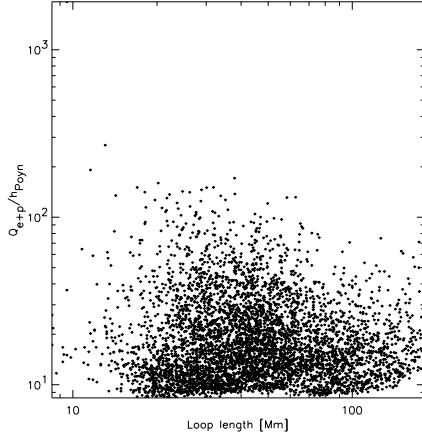


Fig. 8.— Ratio of the heating rates due to particles over  $h_{Poynt}$ , the energy rate corresponding to the Poynting flux.

the ratio of the total heating  $Q_{p+e} = Q_p + Q_e$ , due to electrons and protons, over the value of the Poynting flux function,  $h_{Poynt}$  injected inside the loops, (plotted in Figure 2). We observe that 95% of the values  $Q_{p+e}/h_{Poynt}$ , are in the range of 9 to 50 with an average of 21.

Thus, the heating rate found in our model by consideration of particle acceleration overestimates the one induced by the value of the Poynting flux by an average factor  $\simeq 20$ . This appears at first as a large inconsistency. However, as pointed out in Rosdahl and Galsgaard (2010) or Birn and Priest (2007) (p. 287) this inconsistency should be regarded as a consequence of the inherent lack of self-consistency in all methods estimating particle acceleration via the trajectories of test particles. In fact, in MHD simulations of coronal heating (Hendrix *et al.* 1996; Galsgaard & Nordlund 1996; Rappazzo *et al.* 2007) one finds  $Q_{p+e}/h_{Poynt} \simeq 1$ . However, in such simulations the balance is restored partly due to an additional feedback mechanism caused by the on-going twisting and relaxation of magnetic fields. On the other hand the effects of magnetic reconnection on the acceleration of particles cannot be captured by such simulations. At any rate, our present results show that the thermalization of the loops is indeed possible, at least as shown by order of magnitude estimates, via the conversion of magnetic energy to particles' kinetic

energy during magnetic reconnection.

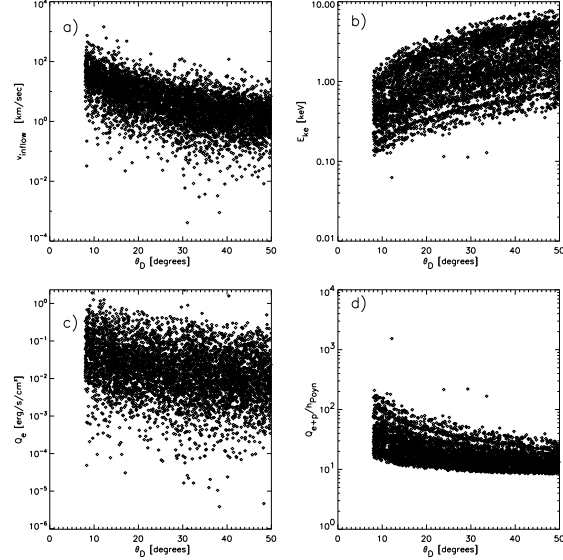


Fig. 9.— Some key quantities of our model as a function of  $\theta_D$ . Panel a) shows the  $v_{inflow}$  velocity, panel b) shows the final kinetic energy of electrons, panel c) shows the heating due to the accelerated electrons and panel d) the ratio of heating due to accelerated electrons and protons over the heating corresponding to the supplied Poynting flux. In all panels, the horizontal axis shows  $\theta_D$  values for each loop.

One more feature to notice is that a possible lifetime of a single current sheet could be of the order of the Alfvén crossing time, which is equal to the fraction of the current sheet length over the Alfvén speed (Klimchuk 2006). In our model this time ranges from 1 s to 135 s. On the other hand, hydrodynamic simulations of nanoflares consider storm of many nanoflares with a duration of 50 s to 500 s (Klimchuk 2006). Let us note that the ratio  $V_{rec}/V_{loop}$  is less than 1 for 95% of our current sheets, if we set their lifetimes equal to the Alfvén crossing time. This means that for a 5% of the loops, reconnection would end practically because of the lack of sufficient plasma inflow. For the other cases, only a fraction of the total number of particles stored in each loop was able to cross the current sheet during the reconnection event. Moreover, the time needed for an individual particle to cross the current sheet is much smaller than

any of the above time scales. For electrons, the particle acceleration time is in the range  $10^{-6}$  s to 0.01 s while for protons it is in the range  $10^{-4}$  s to 1 s. In 98% of cases the acceleration times of protons turn to be smaller than one tenth of the corresponding current sheet lifetime. This justifies our assumption that the particles interact with a quasi-stationary environment during the acceleration phase.

An additional remark is that our computed accelerated particles' kinetic energies and heating functions are still valid if, instead of a monolithic current sheet per loop, we assumed a large number of current sheets, as long as these sheets are formed by the same discontinuity angle  $\theta_D$ , the same magnetic field components  $B_{rec}, B_{\perp}, B_{\parallel}$ , the same thickness and they are longer than the corresponding acceleration length  $z_{max}$ . Moreover, we only consider particles interacting with only one current sheet during their travel inside the loop. Thus Equation (13) describes the heating per current sheet which is proportional to a fraction  $S_{foot}A_{phot}$  of the heating rate supplied. In Section 8 we will calculate the hydrodynamic response of the studied loops under the effect of a number of current sheets producing the same collective heating effect with the one described by Equation (13).

To summarize the results of Sections 5 and 6, Figure 9, shows some model parameters as a function of  $\theta_D$ . These parameters were presented in previous figures as a function of the loop length. The inflow velocity  $v_{inflow}$ , (Fig. 9a) has higher

values for a lower  $\theta_D$ . In Fig. 9b, the kinetic energies of electrons decrease with increasing  $\theta_D$  according to Eq. 12, where the first term in the last sum depends on  $\sin \theta_D$ . On the other hand,  $Q_e$  is higher for lower  $\theta_D$  (Fig. 9c), as expected from Eq. 15. Finally, in Fig. 9d one can see that for higher  $\theta_D$ ,  $Q_{e+p}/h_{Poynt}$  tends asymptotically to a lower limit  $\simeq 8$ .

We also calculated  $\theta_D$  according to a scaling law given in Eq. 10 in Rappazzo *et al.* (2007). The main parameter in this equation is the ratio of photospheric velocity  $v_{ph}$  over the alfvénic velocity  $v_A$ . For our data, the derived  $\theta_D$  were in all cases less than  $4^\circ$ . The small  $\theta_D$  values are due to the low ratio of photospheric over alfvénic velocities in our model. Alfvén velocities are high due to the low  $n_e$  calculated using the scaling law of Rosner *et al.* (1978) with a relatively low temperature of  $10^6$  K. As shown in Fig. 9, such small  $\theta_D$  values correspond to even larger  $Q_{e+p}/h_{Poynt}$  ratios. However, as pointed out in Rappazzo *et al.* (2007), Eq. 10 should be regarded only as a lower limit of the Parker angle, as it does not take into account the current sheet formation. On the other hand, much higher values of  $\theta_D$  are predicted in Hendrix *et al.* (1996); Galsgaard & Nordlund (1996).

## 7. Average thick target X-ray spectrum from nanoflares

In this section we attempt to model the expected form of the thick target spectrum produced by the electrons in the active region loops. We first calculate the distribution of the accelerated electrons' kinetic energy. The total number of electrons,  $N_e$ , produced by each loop is given by the product of the loop electron density  $n_e$  (given by Rosner *et al.* (1978)) multiplied by the plasma volume  $V_{rec}$  entering the current sheet during the reconnection time  $t_{rec}$ . Therefore,  $N_e = 2v_{inflow}t_{rec}n_eA_{rec}$ . We assume that the kinetic energy distribution in each loop lies in the energy range  $\Delta E = [E_{kin(min)}, E_{kin(max)}]$ , where  $E_{kin(min)}$  and  $E_{kin(max)}$  are the energy limits calculated by Equation (9). The amplitude of the kinetic energy distribution of each loop is equal to  $g = N_e/\Delta E$  and is assumed to be constant inside  $\Delta E$ . To compute the kinetic energy distribution of all selected loops, we divide the

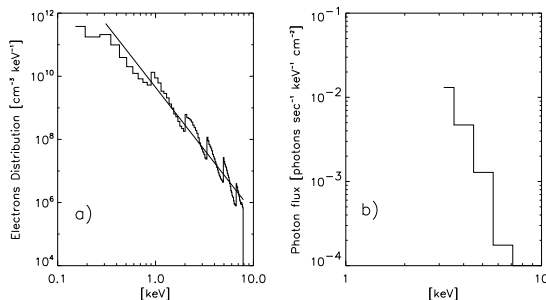


Fig. 10.— Average kinetic energy distribution from the 5000 selected loops (panel a) and the corresponding X-ray spectrum (panel b) calculated according to the thick target approximation.

energy  $E$  from 0.1 keV to 7 keV in 100 energy bins of  $\delta E = 0.07$  keV. For each energy bin, at a given energy  $E$ , we take the sum of the individual loop distribution amplitudes  $g_j$  for which  $(E_{kin(min)j} < E < E_{kin(max)j})$ . Also, for each energy bin we take the sum of the volumes  $V_{loopj}$  of the corresponding loops. Finally, the average kinetic energy distribution  $F(E)dE$  is calculated at each energy bin  $i$  as  $F(E_i) = \Sigma g_j / \Sigma V_{loopj}$ , in units of (electrons  $\text{cm}^{-3} \text{keV}^{-1}$ ). Note that this distribution assumes that nanoflares from all loops are triggered simultaneously, which is one more simplification. Our derived active region kinetic energy distribution is shown in Figure 10a. We performed a power law fit of the form  $F = GE^b$  and found an exponent  $b \simeq -4$  and a proportionality factor  $G = 3.3 \times 10^9 \text{ cm}^{-3} \text{keV}^{-1}$ . We used the derived fit parameters to compute the X-ray spectrum assuming the thick target approximation (Brown, 1971) using the Fortran code developed by Holman (Holman 2001). We assumed that the area of the radiating source function equals the sum of the loop footpoints areas which is  $A = 7 \times 10^{19} \text{ cm}^2$ . The resulting X-ray spectrum is seen in Figure 10b. The X-ray spectrum is divided by the number of loops (5000) assuming that on average only one nanoflare is active at a time. Therefore, the computed X-ray represents a lower limit of the nanoflare emission. The computed X-ray flux per loop has a maximum at 3 keV, of value  $10^{-2} \text{ photons s}^{-1} \text{keV}^{-1} \text{cm}^{-2}$ , and falls at  $10^{-4} \text{ photons s}^{-1} \text{keV}^{-1} \text{cm}^{-2}$ , at 7 keV. Our derived X-ray spectrum exhibits a narrow energy range because of the narrow energy range of the electron kinetic energies. For this reason, a comparison of the spectrum shape with low solar activity X-ray observed spectra, as the RHESSI data presented in McTiernan (2009), or the SphinX data present in Miceli *et al.* (2012) was not attempted. However, our computed X-ray flux is of the same order of magnitude as the upper limits measured in the quiet Sun with RHESSI, (Hannah *et al.* (2011), their Figure 12, left panel, page 278).

## 8. Loop hydrodynamic response to nanoflares

In this section, we employ the heating rates computed via Eq. 13 as an input to hydrodynamic loop simulations. This allows to determine the thermal response (differential emission measure;

DEM) to the heating resulting from our model. As the DEM can be deduced also by observations, comparison between simulated and observed DEMs is a standard test-bed for coronal models.

We assume that each loop is heated due to the activation of several current sheets of sub-telescopic sizes, which inject beams of accelerated particles into the loops. Each current sheet is activated for a duration of the order of the Alfvén crossing time along the loop, but the nanoflare cascade duration is different and subject to parametrization.

We also assume that after the particles (electrons and protons) are accelerated somewhere along the loop, they exit the current sheet, and they deposit their kinetic energy, via Coulomb collisions, to the lower and denser parts of the loop (i.e., thick-target model of electron beams; e.g. Brown, (1971)). However, the general characteristics (e.g. maximum temperature and density), of loops submitted to thermal (i.e., direct) and non-thermal (i.e., particle) heating do not substantially differ for the same total energy release (e.g. Warren & Antiochos (2004)). Differences could arise in the ultra-hot plasma ( $> 5$  MK), during the early stages of impulsive heating (e.g. Klimchuk *et al.* (2008)) or in the mass flows from the loop footpoints, which are however not considered here. Instead, particle heating is treated here as thermal heating. Finally the particle beams follow the magnetic field lines directly connected to their individual current sheet whereas the macroscopic loop is heated due to the collective effect of all individual current sheets.

In order to study the loop plasma response to the calculated heating rates we use the EBTEL model of Klimchuk *et al.* (2008). EBTEL is a 0D model, i.e. it considers spatially-averaged properties, and uses analytical approximations to solve the time-dependent hydrodynamic equations. It was found in good agreement with simulations using far more complex, yet computationally expensive, 1D models. By definition then, the heating is assumed to be spatially uniform in EBTEL. Allowing for different scenarios of the spatial localization of the heating leaves distinct signatures only during the early stages of the hydrodynamic evolution, when the loop is at very high temperatures (e.g. Patsourakos & Klimchuk (2005)). For a given heating profile, loop length, and initial

temperature and density conditions, EBTEL calculates at any instance the coronal temperature and density as well as the transition region (foot-point) and coronal DEM. The application of our model to the observations of NOAA 09114 described in the previous paragraphs supply to each loop hydrodynamic simulation the length and the corresponding heating rate. Given that the model is 0D and analytical, it can calculate numerous solutions within feasible computer times.

Our hydrodynamic calculation starts with initial conditions determined according to the scaling law of to Rosner *et al.* (1978), at a coronal temperature of 1 MK. (However note that this scaling law is derived in the hydrostatic limit. For the use of this approximation see our Section 9). Then, and corresponding to  $t=0$  s, each loop was submitted to impulsive heating, given by Equation 13, so that each loop is heated impulsively by the corresponding heating rate of Figure 7. The heating took the form of a step function, with a duration of  $t_{heat}$ . Numerical simulations (Georgoulis *et al.* 1998) predict a wide distribution for the duration of heating events in nanoflares. Therefore,  $t_{heat}$  is a free parameter for our model, and we run simulations with the values  $t_{heat} = 15$  s, 50 s, 100 s, 250 s, and 500 s, for all the loops. We also considered the case of  $t_{heat}$  set equal to the Alfvén crossing time for each loop. Since  $t_{heat}$  is in general longer than the Alfvén crossing time, this computation can correspond to a storm of nanoflares when the different fragments of the loop current sheet are activated at different times. The employed  $t_{heat}$  values are compatible with the duration of small-scale impulsive energy release events found in MHD simulations of coronal heating. For each loop the corresponding simulations lasted for 5000s to allow both the heating and cooling of plasma to be followed.

In Figure 11, we plot the histogram of the temperatures of the peak of the temporally-averaged DEM of each loop computed for  $t_{heat}=100$  s. In Fig. 11, the vertical axis represents the number of loops per temperature bin. We can see that the particle heating creates an almost uniform distribution of temperatures. The peak of the distribution at  $10^6$  K corresponds to loops not significantly influenced by the heating and keeping their initial temperature. For  $t_{heat} = 50$  s the temperatures histogram is very similar to the one of

Fig. 11. For  $t_{heat} = 500$  s, the distribution exhibits a plateau in the range of 2 MK up to 7 MK, while for  $t_{heat} = 15$  s, the histogram shows a higher probability of temperatures lower than 2 MK.

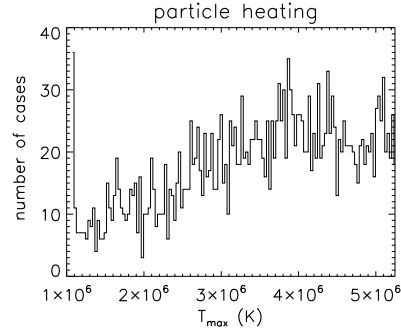


Fig. 11.— Histogram of temperatures achieved at the maximum of each loop time-averaged DEM distribution. This calculation is performed for  $t_{heat} = 100$  s.

In Figure 12 we plot the time-averaged DEMs for all the considered loops in NOAA AR 09114. The plotted DEMs correspond to both the coronal and footpoint parts of the modeled loops. This is legitimate because we deal with averages over the entire AR which would obviously include contributions from both the coronal and footpoint regions. The latter are known to supply, particularly in AR cores, most of the low temperature emission at around 1 MK.

DEMs provide the amount of plasma present at each temperature bin and therefore offer an idea of the thermal distribution of the region or feature in question. Several remarks are now in order from Figure 12. The deduced DEMs has maximum values  $9 \times 10^{20}$ ,  $2 \times 10^{21}$ ,  $4 \times 10^{21}$ ,  $10^{22}$  and  $1.5 \times 10^{22} \text{ cm}^{-5} \text{ K}^{-1}$  for  $t_{heat}$  of 15, 50, 100, 250, and 500 s respectively. The temperature of the maximum DEM value raises for higher heating durations and it is found in the range of 6.4 to 6.6. in  $\log(T)$ .

Observationally deduced DEMs (e.g. Landi and Landini (1997); O'Dwyer *et al.* (2011): their Figures 4 and 14 respectively) exhibit a broad peak from 6-6.5 in  $\log$  of  $T$  at a value of few times  $10^{21} \text{ cm}^{-5} \text{ K}^{-1}$ . At both limits of this plateau, DEMs drop off rapidly. Therefore, the DEMs from our model can reproduce the features of observed



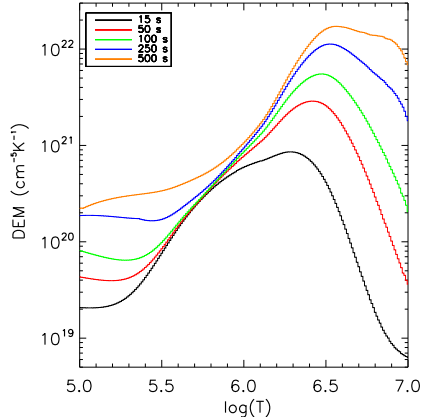


Fig. 12.— Differential Emission measure calculated with the heating caused by particle acceleration calculated for different  $t_{heat}$ .

AR DEMs. Once again we emphasize that, in the framework of our proof-of-concept calculations, we are not aiming to reproduce any particular observational detail.

## 9. Discussion

Since a rather large number of assumptions and/or approximations were introduced in our modeling of nanoflare heating presented in the previous sections, we summarize here the main limitations and conditions of validity of our model, as well as possible future extensions.

### 9.1. Model limitations

An important limitation of our model is that it does not describe the initial process of transformation of photospheric Poynting flux into magnetic free energy, which, when a certain critical value of the Parker angle is reached, is presumably released back into the plasma causing heating. Here, we simply assumed that all loops reach the critical point (Parker angle) at which the Poynting flux is transformed into particle acceleration.

It should be noted that reconnection is a complex non-steady phenomenon (Loureiro *et al.* 2007; Samtaney *et al.* 2007). The presence of a guide magnetic field component has an important influence yet not fully understood (Yamada *et al.* 2010; Birn and Priest 2007). Another important

approximation is the use of a Harris type analytical geometry to study the orbits of accelerated particles. Such an approach does not take into account either the perturbations caused by the accelerated particles onto the fields or the more complex structures of the magnetic field topology that we expect to be formed at the reconnection sites.

The scaling laws of Rosner *et al.* (1978) were presently used in order to compute initial conditions for our nanoflare simulations, as well as for the calculation of kinetic energies and heating rates in the previous sections. However, these formulae are valid in a strict sense for hydrostatic atmospheres, while in reality all parameters in our calculations should exhibit some time dependence. One may remark, nevertheless, that the characteristic timescale of evolution of the atmosphere is determined by the time  $t_{evap}$  needed by the chromospheric evaporation flows to fill the loops with dense and hot plasma. According to some large flare simulations (Yokoyama & Shibata (1998)), chromospheric evaporation flows at 0.2-0.3 of the sound speed, at a temperature  $\simeq 4 \times 10^6$  K. We find  $t_{evap} = L/(0.4 v_s)$  in the range of 100 s to 500 s for 80% of our cases. The resulting time-scales are of the same order with the highest  $t_{heat}$  values used in our calculations. At any rate, Yokoyama & Shibata (1998) argue that the chromospheric evaporation flow should not influence the reconnection rate at a flare's X-point. In view of the above, and since  $t_{evap}$  is typically larger or at most equal to  $t_{heat}$ , we conclude that the use of Rosner *et al.* (1978) scaling laws in our heating computations is an allowable approximation. A more accurate computation would require a proper application of a chromospheric evaporation particle heating rate feedback model. This is proposed for future work.

### 9.2. Comparison with other models

Some words are necessary to explain our choice of hydrodynamic model. There are basically two approaches to study coronal loop heating based on i) 3D MHD (e.g., Gudiksen and Nordlund (2005); Peter, *et al.* (2006); Dahlburg *et al.* (2012); Bingert and Peter (2011)), or ii) 1D and 0D hydrodynamic simulations. 3D MHD simulations supply a physics-based heating function (e.g., Ohmic heating at intense current sheets

formed at the interfaces of braided magnetic elements). However 3D MHD simulations lack the spatial resolution available in 1D hydrodynamic simulations. A high resolution, on the other hand, is crucial for an accurate description of the plasma thermodynamic response to a given heating. Nevertheless, the heating functions selected in 1D hydrodynamic loop simulations is ad-hoc, i.e., they can be chosen arbitrarily. Finally, hydrodynamic descriptions are far less computationally expensive than 3D MHD and thus more appropriate for extensive studies of thousands of loops.

A future improvement could concern the geometry of our model. Replacing the Harris current sheet with a more realistic geometry would allow to calculate test particle orbits for a range of parameters pertinent to solar active regions, over a large number of coronal loops. Of course, the ultimate improvement would be to simulate the feedback of the plasma response due to the chromospheric evaporation on the acceleration of the particles.

## 10. Conclusions

In the present study, we provide a set of calculations for nanoflare heating in coronal loops based on a composite model in which the heating term used for hydrodynamic simulations of nanoflares is provided by considering particle acceleration in reconnecting current sheets. Our main steps and conclusions are the following:

1) Our calculations are utilizing the data of observations: (a) The general structure of the magnetic field is deduced by means of a current-free (potential) magnetic field extrapolation of an observed active region's (NOAA AR 9114) magnetogram. (b) We selected 5000 closed magnetic field lines, derived from the extrapolation, to represent coronal loops in which we will study the nanoflares. (c) Poynting flux is supplied in current sheets, one for each coronal loop, produced by photospheric motions at the loop footpoints. The Poynting flux is calculated using the measured magnetic fields and the estimated values for the inductive velocities at the photospheric level.

2) In our current sheets, reconnection always occurs, because we assume that the discontinuity in the magnetic field configuration has reached a critical mis-alignment angle. The mis-alignment

angle,  $\theta_D$ , (twice the adopted Parker angle) varies randomly from loop to loop in a uniform distribution from  $8^\circ$  to  $50^\circ$ . In this model we compute the physical conditions in the current sheets. The induced electric field  $E_{rec}$  is in the range 0.01 to 100 V/m, and is larger than the Dreicer electric field which favors the direct acceleration of particles. The plasma inflow velocity  $v_{inflow}$  is in the range of 0.1 to 100 km s $^{-1}$ .

3) The Poynting flux supplied by the photospheric motion is entirely transformed into kinetic energy of the particles, accelerated in the reconnecting current sheets. The final kinetic energies of electrons and protons are calculated using analytic formula derived in test particle studies (Efthymiopoulos *et al.* 2005; Litvinenko 1996). The electron kinetic energy gain turn to be up to 8 keV, while for protons it turn to be in the range of 0.3 to 470 keV.

4) We consider the process of particles' acceleration as the unique source of plasma heating. This assumption is supported by the fact that, at least in large flares, electron acceleration corresponds to 50% of the released energy (Birn and Priest 2007). We use a simple phenomenological expression (Eq. 13) to compute the heating rate produced by accelerated electrons  $Q_e$  and protons  $Q_p$ . The produced heating rates are in the range of  $10^{-4}$  to  $1 \text{ erg s}^{-1} \text{ cm}^{-3}$  while the ratio  $Q_p/Q_e$  takes values in the range 0.1 to 5 and is higher than 1 in 50% of cases.

The power law of the computed heating rate as a function of the loop length, derived both via a fit to the calculated data and via an analytical derivation yields an exponent of  $\simeq -1.5$ , which falls within the constraints derived from observations (Mandrini *et al.* 2000). Moreover, we found a linear dependence of the heating functions on the Poynting flux at the footpoints and a trigonometric dependence on the angle  $\theta_D$ .

5) We computed the form of X-ray spectra generated by the accelerated electrons from all loops, using the 'thick target' approach. The derived spectrum has a peak intensity of  $10^{-2} \text{ photons s}^{-1} \text{ keV}^{-1} \text{ cm}^{-2}$  at 3 keV and decreases with a power law shape and an exponent equal to  $\simeq -4$ . This result is in agreement with today upper limits derived from observations (Hannah *et al.* 2011).

6) Finally we performed hydrodynamic simula-

tions using the 0D EBTEL code to compute the characteristic atmospheres of our loops. The constraints of the simulations are the derived heating rates and the loop length while the heating event duration is kept as a free parameter. The deduced DEMs have maximum values in the range of  $9 \times 10^{20}$  to  $1.5 \times 10^{22} \text{ cm}^{-5} \text{ K}^{-1}$  for temperatures from 6.4 to 6.6 in  $\log(T)$ . These derived values are in agreement with DEMs derived from observations (Landi and Landini 1997; O'Dwyer *et al.* 2011).

7) We discuss the various limitations of our model and we propose a number of possible future extensions as well as comparisons with other models in the literature.

**Acknowledgements:** We thank the anonymous referee for helpful and constructive comments. This research has been supported in part by the European Union (European Social Fund ESF) and in part by the Greek Operational Program "Education and Lifelong Learning" of the National Strategic Reference Framework (NSRF) - Research Funding Program: Thales. "Hellenic National Network for Space Weather Research"-MIS 377274. S.P. acknowledges support from an FP7 Marie Curie Grant (FP7-PEOPLE-2010-RG/268288). C.G. acknowledges support from program 200/790 of the research committee of the Academy of Athens.

## REFERENCES

- Alissandrakis, C.E., 1981, *Astron. Astrophys.*, 100, 197
- Anastasiadis, A., Gontikakis, C., Efthymiopoulos, C., 2008, *Sol. Phys.*, 253, 199
- Benz, A.O., 'Plasma Astrophysics' 1993, Kluwer Academic Publishers, ISBN-0-7923-2429-3
- Bingert, S., Peter, H., 2011, *Astron. Astrophys.*, 530, 112
- Birn, J., Priest, E., 2007, 'Reconnection of magnetic fields' Cambridge University Press, ISBN-13 978-0-521-85420-7
- Brown, J. C., 1971, *Solar Phys.*, 18, 489
- Cassak, P.A., Drake, J.F., Shay, M.A., 2007, *Phys. Plasmas*, 14, 054502
- Cassak, P.A., Mullan, D.J., Shay, M.A., 2008, *ApJ*, 676, 69
- Chen, B., Bastian, T.S., White, S.M., Gary, D.E., Perley, R., Rupen, M., Carlson, B., 2013, *ApJ*, 763, 21.
- Cirtain, J.W., Golub, L., Winebarger, A.R., De Pontieu, B., Kobayashi, K., Moore, R.L., Walsh, R.W., Korreck, K.E., Weber, M., McCauley, P., Title, A., Kuzin, S., DeForest, C.E., 2013, *Nature*, 493, 501
- Dahlburg, R.B.; Klimchuk, J.A.; Antiochos, S. K., 2005, *ApJ*, 622, 1191
- Dahlburg, R.B., Liu, J.-H., Klimchuk, J.A., Nigro, G., *ApJ*, 704, 1059
- Dahlburg, R.B., Einaudi, G., Rappazzo, A.F., Velli, M., 2012, *Astron. Astrophys.*, 544, 20
- Dreicer, H., 1959, *PhRv*, 115, 238
- Eastwood, J.W., 1972, *Planetary Space Sci.*, 20, 1555
- Efthymiopoulos, C., Gontikakis, C., Anastasiadis, A., 2005, *Astron. Astrophys.*, 443, 663
- Emslie, A.G., Hénoux, J.-C., Mariska, J.T., Newton, E.K., 1996, *ApJ*, 470, 131
- Galsgaard, K., Nordlund, 1996, *JGR*, 101, 13445
- Georgoulis, M. K., Velli, M., Einaudi, G., 1998, *ApJ*, 497, 957
- Georgoulis, M. K.; LaBonte, B. J.; Metcalf, Thomas R., 2004, *ApJ*, 602, 446
- Georgoulis, M.K., 2005, *ApJ*, 629, 69
- Georgoulis, M., LaBonte, B.J., 2006, *ApJ*, 636, 475
- Georgoulis, M.K., 2012, *Solar Phys.*, 276, 423
- Gontikakis, C., Efthymiopoulos, C., Anastasiadis, A., 2006, *MNRAS*, 368, 293
- Gontikakis, C., Anastasiadis, A., Efthymiopoulos, C., 2007, 378, 1019
- Gontikakis, C., Contopoulos, I., Dara, H.C., 2008, *Astron. Astrophys.*, 489, 441

- Gudiksen, B.V., Nordlund, Å, 2005, *ApJ*, 623, 600
- Handy, B. N., Bruner, M.E., Tarbell, T.D., Title, A. M., Wolfson, C.J., Laforce, M.J., Oliver, J.J., 1998, *Solar Phys.*, 183, 29
- Hannah, I.G., Hudson, H.S., Battaglia, M., Christe, S., Kasparova, J., Krucker, S., Kundu, M.R., Veronig, A., 2011, *Space Sci. Rev.*, 159, 263.
- Harra, L.K., Archontis, V., Pedram, E., Hood, A.W., Shelton, D.L., van Driel-Gesztelyi, L., 2011, *Solar Phys.*, DOI: 10.1007/s11207-011-9855-x
- Hendrix, D.L., Van Hoven, G., Mikic, Z., Schnack, D.D., 1996, *ApJ*, 470, 1192
- Hesse, M., Schindler, K., Kuznetsova, M., 1999, *Phys. Plasmas*, 6, 1781
- Holman G.D., 2001, web-cite hesperia.gsfc.nasa.gov/hessi/modelware
- Klimchuk, J.A., 2006, *Solar Phys.*, 234, 41
- Klimchuk, J.A., Patsourakos, S., Cargill, P.J., 2008, *ApJ*, 682, 1351
- Landi, E., Landini, M., 1997, *Astron. Astrophys.*, 327, 1230
- Lemen, J.R., Title, A.M., Akin, D.J., Boerner, P.F., Chou, C., Drake, J.F., Duncan, D.W., Edwards, Ch.G., Friedlaender, F.M.; Heyman, G.F., *et al.* 2012, *Solar Physics*, 275, 17
- Litvinenko Y.E., Somov B., 1993, *Solar Phys.*, 146, 127
- Litvinenko Y.E., 1996, *ApJ*, 462, 997
- Litvinenko Y.E., 2000, *Solar Phys.*, 194, 327
- Loureiro, N.F., Schekochihin, A.A., Cowley, S.C., 2007, *Phys. Plasmas*, 14, 100703
- O'Dwyer, B., Del Zanna, G., Mason, H. E., Sterling, A. C., Tripathi, D., Young, P. R., 2011, *Astron. Astrophys.*, 525, 137
- Mandrini, C.H., Demoulin, P., Klimchuk, J.A., 2000, *ApJ*, 530, 999
- Martens, P.C.H., Young, A., 1990, *apjs*, 73, 333
- McTiernan, J.M., *ApJ*, 697, 94
- Metcalf, T. R., Leka, K. D., Barnes, G., Lites, B. W., Georgoulis, M. K., Petsov, A. A., Balasubramaniam, K. S., Gary, G. A., Jing, J., Li, J., *et al.*, 2006, *Solar Phys.*, 237, 267
- Mickey, D.L., Canfield, R.C., Labonte, B.J., Leka, K.D., Waterson, M.F., Weber, H.M., 1996, *Solar Phys.*, 168, 229
- Miceli, M., Reale, F., Gburek, S., Terzo, S., Barbera, M., Collura, A., Sylwester, J., Kowalinski, M., Podgorski, P., Gryciuk, M., *Astron. Astrophys.*, 544, 139
- Parker, E., 1972, *ApJ*, 174, 499
- Parker, E., 1988, *ApJ*, 330, 474
- Patsourakos, S., Klimchuk, J.A., MacNeice, P.J., 2004, *ApJ*, 603, 322
- Patsourakos, S., Klimchuk, J.A., 2005, *ApJ*, 628, 1023
- Peter, H., Gudiksen, B.V., Nordlund, Å, *ApJ*, 638, 1086
- Priest, E., Heyvaerts, J. F., Title, A., *ApJ*, 2002, 576, 533
- Rappazzo, A.F., Velli, M., Einaudi, G., Dahlburg, R. B., 2008, *ApJ*, 657, 47
- Rosdahl, K.J., Galsgaard, K., 2010, *Astron. Astrophys.*, 511, 73
- Rosner, R., Tucker, W.H., Vaiana, G.S., *ApJ*, 1978, 220, 643
- Samtaney, R., Loureiro, N.F., Uzdensky, D.A., Schekochihin, A.A., Cowley, S.C., 2009, *Phys. Rev. L.*, 103, 105004
- Speiser, T.W., 1965, *J. Geophys. Res.*, 70, 4219.
- Warren, H. P., Antiochos, S. K., 2004, *ApJ*, 611, 49
- Yamada, M., Cruskud, R., Li, H., 2010, *Rev. Mod. Phys.*, 82, 603.
- Yokoyama T., Shibata, K., 1998, *ApJ*, 494, 113